Nitrogen-Doped Holey Graphene as an Anode for Lithium-Ion Batteries with High Volumetric Energy Density and Long Cycle Life

Jiantie Xu, Yi Lin, John W. Connell,* and Liming Dai**

Owing to its high intrinsic electrical conductivity, excellent mechanical flexibility, and exceptionally large theoretical surface area of 2630 $m^2 g^{-1}$, graphene has received significant attention as an anode for lithium-ion batteries (LIBs).[1–3] Because of the strong van der Waals interactions between graphene sheets, however, they tend to restack or aggregate during the process of electrode preparation. The restacking or agglomeration of the graphene sheets severely decreases their accessible surface area and thereby impede ion transport, leading to a low energy density and poor rate capability.[4] Recently, electrodes based on graphene with a large amount of holes in its planar sheet, i.e., holey graphene (hG), have been demonstrated to deliver a high energy (gravimetric/volumetric) density and high rate capability in LIBs[5–7] or supercapacitors.[8–11] The presence of holes in the graphene basal plane could be beneficial to keep the hG nanosheets in the stacks remaining exfoliated. The exfoliated hG allows the electrolyte to quickly penetrate the entire hG cross-planes through the holes as well as to facilitate rapid diffusion and storage of ions. Furthermore, the introduction of in-plane vacancy defects (pores rich with edges) in hG provides an additional advantage for LIBs as the graphene edge has been demonstrated to show a much faster electron transfer rate and higher electrochemical activity than those of the graphene basal plane.[12]

To date, there have been several reports on the preparation of hG as an anode for LIBs.[5–7] For example, pores were introduced into graphene using sonication of graphite oxide (GO) in HNO_3.[5] A porous sponge-like structure composed of randomly stacked hG was prepared through a hydrothermal method followed by etching with KOH and ball milling.[6] Nitrogen-doped hG hollow microspheres were synthesized through a template sacrificing method using amine-functionalized mesoporous silica nanoparticles as a template.[7] Such hollow microspherical structures, in combination with the introduction of nitrogen doping, effectively facilitated lithium-ion storage and transport, and thus resulted in enhanced electrochemical performance. However, the use of hollow microsphere structures would significantly reduce the volumetric energy density. Moreover, its preparation methods, along with other reported methods of hG for LIBs, are either not scalable or involve the use of toxic or hazardous chemicals. Very recently, Lin et al.[13] directly heated commercially available graphene in air without any catalysts or chemicals to produce hG in a scalable process. Compared to other reported methods,[5–7,14] this method is more scalable and facile, and does not use toxic chemicals.

The introduction of heteroatoms (e.g., nitrogen) to graphene has been proven to be one of the most promising methods to further enhance the capacity, surface wettability, and electrical conductivity of graphene.[7,15,16] To exploit the N-doping effects in different graphene materials, we prepared a series of graphene (G), N-doped G (N-G), hG, and N-doped hG (N-hG), as anodes for LIBs. We found that N-hG anode for LIB prepared by simply heating hG in ammonia gas exhibited a high volumetric capacity of 384 mAh cm^{-3} at 0.1 A g^{-1}, a maximum volumetric energy density of 171.2 Wh L^{-1}, and a maximum volumetric capacitance of 201.6 F cm^{-3} at 5 A g^{-1} during the 6000 cycles tested. The volumetric energy and capacitance of N-hG are higher than those of the other three types of graphene, and highly comparable to the best results previously reported for capacitors based on carbon electrode materials in organic electrolytes.[8,10] The excellent electrochemical performance of N-hG was attributed to a synergistic effect of nitrogen doping and holes to provide high electrical conductivity, reduced effective diffusion distance, numerous active sites for Li^+ storage, high wettability, and low charge-transfer resistance between

Dr. J. Xu, Prof. L. Dai
Department of Macromolecular Science and Engineering
Case Western Reserve University
10900, Euclid Avenue, Cleveland, OH 44106, USA
E-mail: liming.dai@case.edu

Dr. Y. Lin
National Institute of Aerospace
100 Exploration Way, Hampton, VA 23666, USA
E-mail: yi.lin@nianet.org

Dr. Y. Lin
Department of Applied Science
The College of William and Mary
Williamsburg, VA 23185, USA

Prof. J. W. Connell
Mail Stop 226
Advanced Materials and Processing Branch
NASA Langley Research Center
Hampton, VA 23681, USA
E-mail: john.w.connell@nasa.gov

DOI: 10.1002/smll.201501848

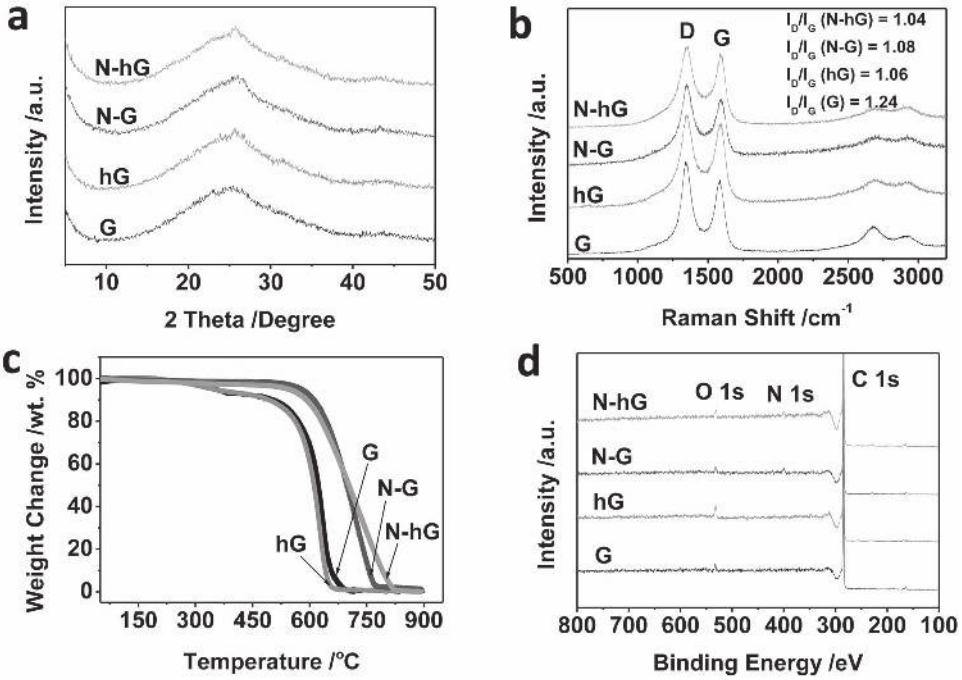

Figure 1. a) XRD patterns; b) Raman spectra; c) TGA curves (10 °C min^{-1}; 60 vol% compressed air in N_2); and d) XPS spectra of G, hG, N-G, and N-hG.

the electrolyte–electrode interface. Furthermore, it is envisioned that the malleable amorphous structures can more readily accommodate the local volume change during the lithiation–delithiation process. Indeed, our results indicate that N-hG with a high packing density and excellent ion transport/storage serves as an ideal anode material for LIBs with high energy densities (both gravimetric and volumetric) and ultralong cycling life.

Figure 1a shows broadened X-ray diffraction (XRD) peaks at ≈26.5° for all the G, hG, N-G, and N-hG samples, indicating their partially crystalline structures with a typical interlayer space of 0.34 nm between graphene nanosheets. Due to the heat treatment of hG under different atmospheres (air and ammonia gas), the resultant products will likely exhibit a different degree of exfoliation, nitrogen doping levels, defects, and hole size and distributions for hG, N-G, and N-hG. Figure 1b shows Raman spectra for G, hG, N-G, and N-hG; all revealed a pronounced D band (a disordered band caused by the graphite edges) at around 1349 cm^{-1} and a G band (associated with in-plane vibration of the graphite lattice) at around 1591 cm^{-1}. Compared to that of G (1.24), the intensity ratios of the D and G bands (I_D/I_G) for hG (1.06), N-G (1.08), and N-hG (1.04) were significantly reduced, presumably due to the defect removal through the combined effects of nitrogen-doping and high-temperature treatment. This is further confirmed by the absence of the distinct weight losses in the thermogravimetric analysis (TGA) for N-G and N-hG with respect to G and hG in the temperature range of 300–500 °C (Figure 1c).

To investigate the chemical structure of the samples, the X-ray photoelectron spectroscopic (XPS) survey spectra of G, hG, N-G, and N-hG are displayed in Figure 1d, which shows a pronounced C 1s peak at about 285 eV, along with a much weaker O 1s peak at 534 eV (3.9 at% for G, 6 at% for hG, 2.9 at% for N-G, and 3.5 at% for N-hG) as well as a weak, but noticeable, N 1s peak at about 398 eV (1 at% for N-G, 1.1 at% for N-hG). As can be seen in Figure S1a and Table S1 in the Supporting Information, the lower atom ratio of O/C and the existence of nitrogen for N-G and N-hG indicate, once again, the reduction of oxygen functional groups in consistence with the Raman and TGA results. To further identify the state of C, O, and N, high-resolution XPS spectra for the representative N-hG are presented in Figure S1b–d (Supporting Information), respectively. As expected, the C1s XPS peak (Figure S1b, Supporting Information) can be deconvoluted into a dominant component for sp^2-C at 284.3 eV, along with two weaker bands associated with C—O and C—N at 284.8 eV and O=C—OH at 289.8 eV. The corresponding O1s spectrum (Figure S1c, Supporting Information) shows C=O and C—O peaks at 531.9 and 534.1 eV, respectively. The high resolution XPS N1s spectra of the N-hG (Figure S1d, Supporting Information) can be deconvoluted into three peaks at 398.3, 400.2, and 404.1 eV corresponding to the pyridinic nitrogen, pyrrolic nitrogen, and pyridine-N-oxide, respectively.[17]

To examine the morphology of G, hG, N-G, and N-hG, high-resolution scanning electron microscopic (SEM) imaging was performed. As expected, there is a large amount of holes present on the surfaces of the graphene layers (**Figure 2**b; Figure S2b, Supporting Information) after heating G (thermally exfoliated graphene) with numerous noncrystalline regions on the graphene basal planes (Figure 2a; Figure S2a, Supporting Information) in air.[8] After the nitrogen doping of G and hG by heating under NH_3/Ar, the morphologies of G (Figure 2c; Figure S2c, Supporting Information) and hG (Figure 2d; Figure S2d, Supporting Information) are still preserved.

Figure 3a shows the initial discharge–charge profiles for the G, hG, N-G, and N-hG at 0.1 A g^{-1} in the voltage range

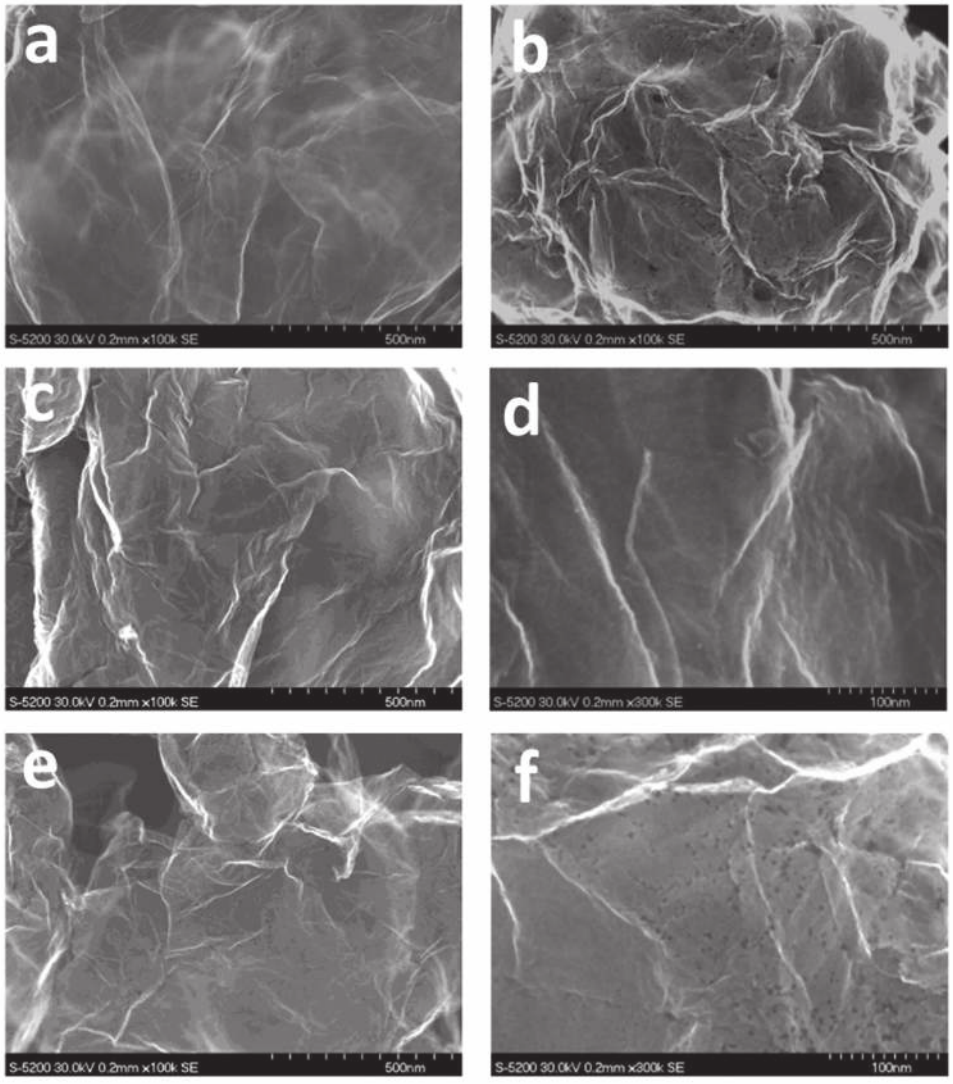

Figure 2. SEM images of a) G, b) hG, c,d) N-G, and e,f) N-hG. Scale bar: a–c,e) 500 nm and d,f) 100 nm.

of 0.02–2.5 V. The discharge–charge profiles are in accordance with the cyclic voltammetry (CV) analysis given in Figure S3 (Supporting Information), which shows the CV curves of the initial three cycles for G, hG, N-G, and N-hG at a scan rate of 0.2 mV s^{-1} in the voltage range of 0.02–2.5 V. As can be seen in Figure S3 (Supporting Information), the first cathodic peak centered at around 0.6 V, corresponding to the flat plateau at around 1 V in Figure 3a, appeared in the first cycle and then disappeared in the following cycles. This indicated that a dense solid electrolyte interphase (SEI) layer from the electrolyte decomposition was formed on the sample surfaces in the first cycle. The second cathodic peak centered at around 0.2 V is mainly ascribed to lithium-ion insertion into the graphitic layers, which is an important indicator of lithium storage in graphene. To test the rate and cycling performance, the cells based on the G, hG, N-G, or N-hG anodes were measured for 60 cycles from 0.1 to 10 A g^{-1} in the voltage range of 0.02–2.5 V (Figure 3b). As can be seen, the N-hG anode showed the highest initial discharge/charge capacity of 3056.1/989.5 mAh g^{-1} at 0.1 A g^{-1}, followed by the N-G (2901.3/852.3 mAh g^{-1}), and then the hG (2732.0/590.4 mAh g^{-1}) and G (1934.5/368.2 mAh g^{-1}), with the corresponding initial Coulombic efficiencies (CE) of 32.4%, 29.3%, 21.6%, and 19.0%, respectively. Compared to those of G and hG, the higher initial CE for the N-hG and N-G are attributable to the fewer oxygen-containing (O-X) functional groups, as well as their higher surface area (vide infra), that effectively decreased the irreversible interaction of lithium and O-X groups during the initial discharge process. Furthermore, by increasing the current density from 0.2 to 10 A g^{-1} and then back to 0.1 A g^{-1}, the N-hG showed a higher reversible capacity and rate capability (Figure 3c) than N-G, hG, and G. As a key parameter for graphene as anode for LIBs, the volumetric capacity of N-hG was estimated in details in Figure S4 (Supporting Information). As expected, the volumetric capacity of N-hG was estimated to be ≈380 mAh cm^{-3}. This value is almost half of the theoretical volumetric capacity of graphite (≈840 mAh cm^{-3}), which only has a theoretical gravimetric capacity of 372 mAh g^{-1}.[18] Moreover, compared to G with ≈49 mAh cm^{-3}, N-hG delivered about seven times higher volumetric capacity. Figure 3d shows discharge–charge curves of N-hG at various current

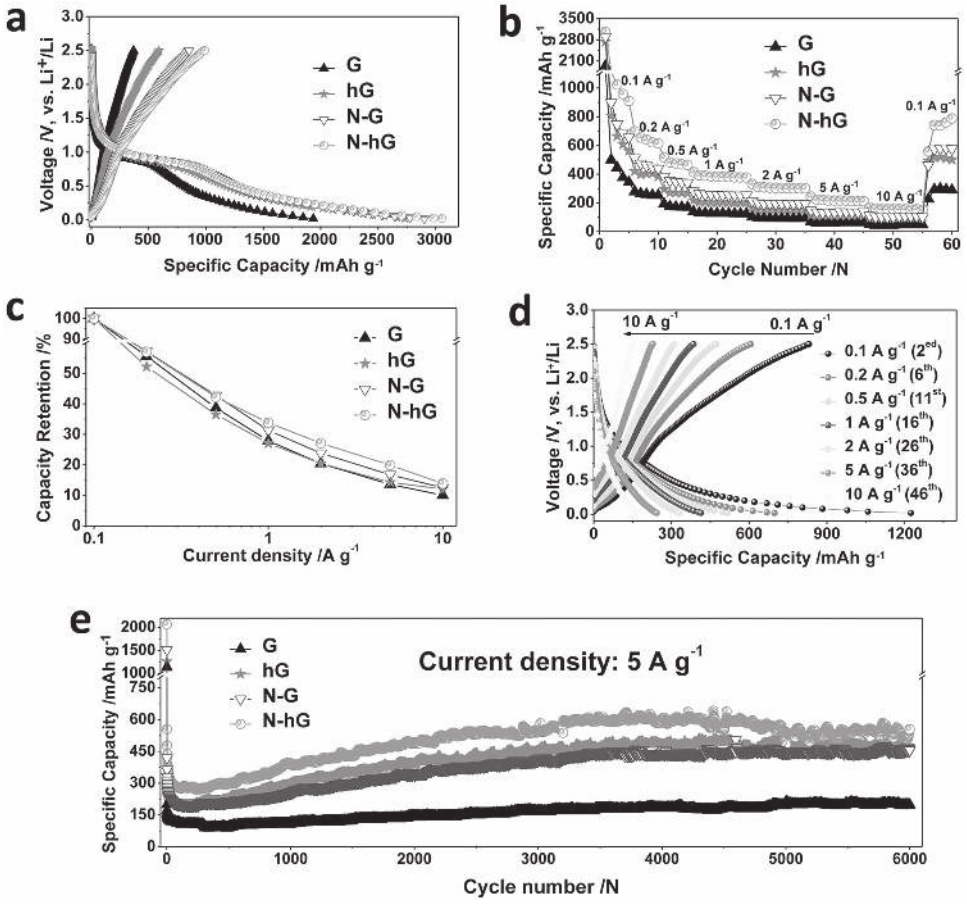

Figure 3. Electrochemical performance of G, hG, N-G, and N-hG measured in the voltage range of 0.02–2.5 V. a) Initial discharge–charge curves at 0.1 A g^{-1}, b) rate capability, c) discharge–charge curves of N-hG at various current densities, d) capacity retention versus various current densities, and e) cycling performance at 5 A g^{-1}.

densities in the voltage range of 0.02–2.5 V. The shapes of the discharge–charge curves, along with Figure 3a, are typical electrochemical behaviors observed with carbonaceous materials.[3,7,19]

To compare the relatively long-term cycling performance of G, hG, N-G, and N-hG, we discharged and charged the cells for 6000 cycles at a high current density of 5 A g^{-1} between 0.02 and 2.5 V. As shown in Figure 3e, N-hG, N-G, hG, and G delivered initial discharge capacities of 2063.8, 1512.6, 1254.2, and 1130.8 mAh g^{-1}, respectively. Although the capacities decreased in the initial cycles, all electrodes exhibited gradually increased capacity in the following cycles until relatively stable values were reached at ≈4000 cycles. This is mainly due to the high electrode polarization at high current densities in the initial cycles resulting from the delay associated with adsorption and wetting of the electrolyte into the electrode materials. With the electrolyte gradually penetrating into the accessible areas of electrode materials during the deep cycling, the electrodes delivered the discharge capacities of 605.4 mAh g^{-1} (N-hG), 439.6 mAh g^{-1} (N-G), 483.8 mAh g^{-1} (hG), and 182.5 mAh g^{-1} (G) at 4000 cycles. Since relatively stable capacity was achieved at around 4000 cycles, the electrodes still retained the discharge capacities of 553.5 mAh g^{-1} (N-hG), 456.1 mAh g^{-1} (N-G), 471.2 mAh g^{-1} (hG), and 198.1 mAh g^{-1} (G) after 6000 cycles. Once again, the higher capacity for N-hG over 6000 cycles demonstrates the superior electrochemical performance of N-hG with respect to N-G, hG, and G.

On the other hand, due to the extraordinary properties of graphene, hG has been demonstrated to be one of the most attractive electrochemical capacitors with a high gravimetric or/and volumetric capacitance.[8,10,11] As shown in **Figure 4**a–g and Figures S5a–g, S6a–g, and S7a–g in the Supporting Information, G, hG, N-G, and N-hG all showed nearly symmetric triangular *V–t* shapes that delivered more attractive capacitances at 5 A g^{-1} in the organic electrolyte of ethylene carbonate (EC)/diethyl carbonate (DEC). Owing to its high operating voltage in EC/DEC electrolyte, N-hG delivered a higher maximum specific energy density of 445.9 Wh kg^{-1} (Figure 4h) and specific capacitance of 525 F g^{-1} (Figure 4i) compared to those of G (237.3 Wh kg^{-1} and 295.8 F g^{-1}) (Figure S5h,i, Supporting Information), hG (361.9 Wh kg^{-1} and 362.5 F g^{-1}) (Figure S6h,i, Supporting Information), and N-G (388.5 Wh kg^{-1} and 453.7 F g^{-1}) (Figure S7h,i, Supporting Information), respectively. In addition, as shown in Figure S4 (Supporting Information), the volumetric energy density and volumetric capacitance of N-hG electrodes at 5 A g^{-1} were estimated to be 171.2 Wh L^{-1} and 201.6 F cm^{-3} (see Section B in Experiments in the Supporting Information), respectively, which were nearly five and three times higher than

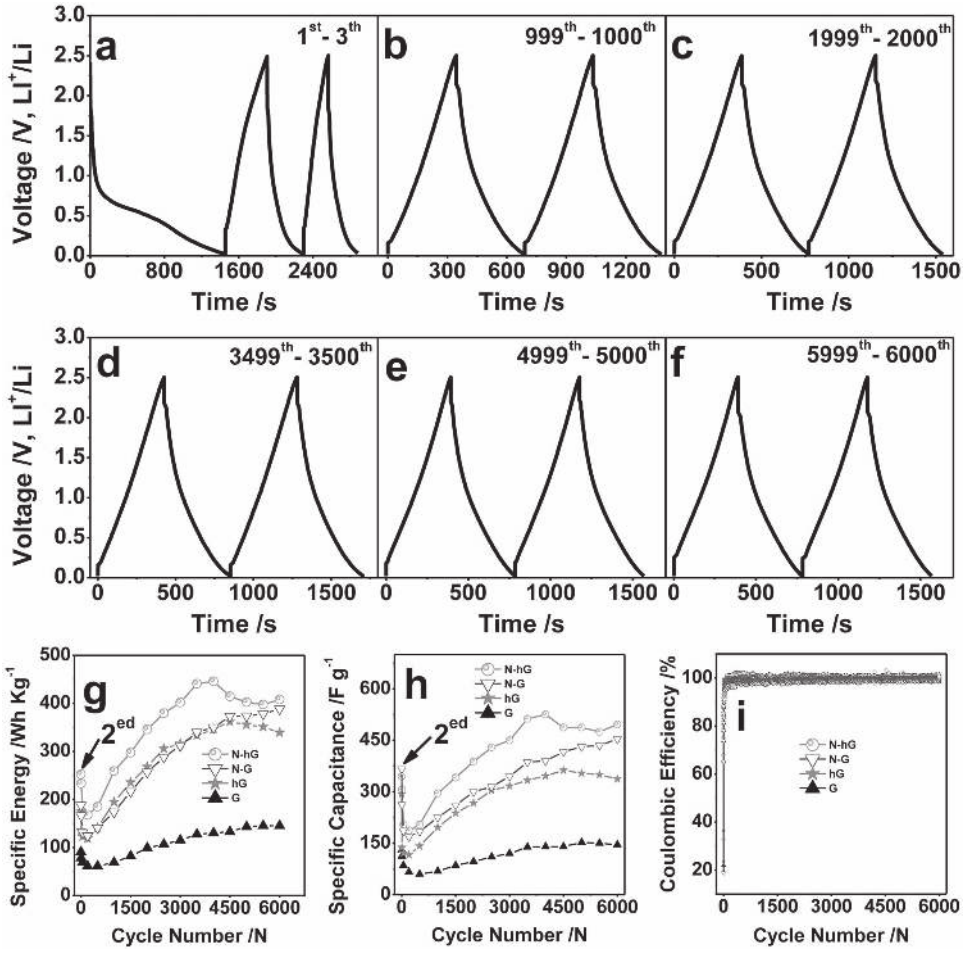

Figure 4. Representative *V–t* curves: a) 1st–3rd, b) 999th–1000th, c) 1999th–2000th, d) 3499th–3500th, e) 4999th–5000th, f) 5999th–6000th for N-hG; g) specific energy, h) specific capacitance, and (i) CE versus cycle number of G, hG, N-G, and N-hG; measured at 5 A g^{-1} in the voltage range of 0.02–2.5 V.

those of G, 31.6 Wh L^{-1} and 39.3 F cm^{-3}, respectively. Both the gravimetric and volumetric values of the N-hG electrode are comparable to the best values reported to date for carbon-based electrodes in capacitors with an organic electrolyte, including activated carbon, carbon nanotubes, and graphene.[8,10,20] Moreover, the CE is often a key indicator for the reversible lithium-ion storage/extraction system. Because of the SEI formation that consumes a certain percentage of the lithium,[2,3,6,7,16,19] G, hG, N-G, and N-hG exhibited the low initial CE. Although G, hG, N-G, and N-hG delivered the relatively low CE in the initial cycles, their CEs rapidly increased up to 100% and remained stable over 6000 cycles (Figure 4j; Figures S5j, S6j, and S7j, Supporting Information), demonstrating the high reversibility of G, hG, N-G, and N-hG electrodes during the long-term storage/extraction process for lithium ions.

To gain a better understanding of the underline factors ensuring the superior electrochemical performance for the N-hG to G, hG, or N-G, we further investigated the key parameters that affect the electrochemical performance of the electrodes for LIBs. First, TGA (Figure 1c) and differential thermogravimetry (DTG) (**Figure 5**a) profiles indicate that the introduction of holes in the graphene sheets slightly reduced the thermal decomposition temperature from 635 °C for G to 624 °C for hG, probably due to the introduction of hole defects and associated oxygen containing functional groups. However, N-doping significantly enhanced thermal stability of the N-G and N-hG, as exemplified by significant increases in the decomposition temperatures from 635 °C for G to 725 °C for N-G, and from 624 °C for hG to 735 °C for N-hG. The enhanced thermal stability for N-hG and N-G can be attributed to the enhanced N—C bonds and the partial removal of O-X functional groups through the doping-induced reduction process. Moreover, as shown in Figure 5b and Figure S8a–d (Supporting Information), the N-hG exhibited a higher Brunauer, Emmett and Teller (BET) surface area of 594.6 m^2 g^{-1} than G (336.8 m^2 g^{-1}), hG (398.9 m^2 g^{-1}), or N-G (457.0 m^2 g^{-1}). The enhanced surface area for the N-hG sample is associated with the presence of nano/mesoholes and defects induced by N-doping (e.g., pyridinic nitrogen, pyrrolic nitrogen, and pyridine-N-oxide). The presence of nano/mesoholes in the holey graphene (hG, N-hG) could not only facilitate the electrolyte diffusion through the hG samples but also effectively increase the accessible area for electrolyte by reducing the restack of graphene sheets, leading to fast diffusion and efficient storage of (lithium) ions.[6,8,10] On the other hand, the presence of nanoholes with doped nitrogen at the edge[21] and doping-induced defects

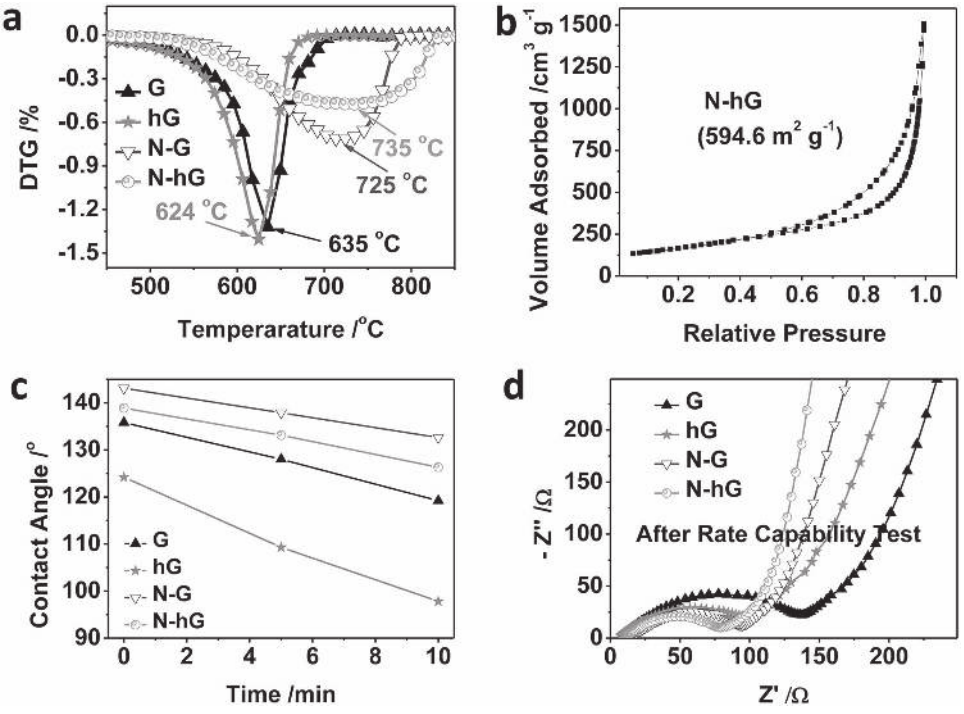

Figure 5. a) DTG at different temperature regions of G, hG, N-G, and N-hG; b) BET nitrogen adsorption and desorption isotherms of N-hG; c) contact angle of water droplets resting on electrodes for 0, 5, and 10 min; and d) EIS spectra of G, hG, N-G, and N-hG after the corresponding rate capability measurement.

at the basal plane in N-hG[22] are expected to provide more active sites for the storage of lithium ions (clusters), and hence an enhanced specific capacity. In addition, oxidized N could also lead to storage of additional lithium ions through the reaction between Li ions and the O-X groups.[23] Compared to G and hG, therefore, the better electrochemical performance observed for N-G and N-hG (N-hG > N-G) could be attributed to a synergistic effect between the nitrogen-doping and the presence of holes to effectively facilitate the diffusion and storage/release of lithium ions.

Different levels of O-X groups and surface area also affect the wettability between electrode and electrolyte, apart from affecting the SEI formation. The wettability of G, hG, N-G, and N-hG electrodes was investigated by measuring the water contact angle using a microliter syringe at room temperature. As shown in Figure 5c and Figure S9 (Supporting Information), N-doping enhanced the hydrophobicity of hG and G, and hence enhanced the wettability for N-hG toward organic electrolyte. The enhanced hydrophobicity is associated with lower contents of —OH and —COOH for the nitrogen-doped graphene (Figure S1a and Table S1, Supporting Information). The improved electrolyte wettability of the N-hG also enhanced the fast diffusion of lithium ions with a low ion-transport resistance and maximized the effective storage of lithium ions during the discharge–charge processes. To better understand kinetics associated with the G, hG, N-G, and N-hG, we performed electrochemical impedance spectroscopic measurements on these samples[24] and showed an equivalent circuit model in Figure S10 (Supporting Information). The equivalent circuit model includes the internal resistance (e.g., electrolyte, contact between the electrode and the corresponding current collector (R_e), resistance for lithium-ion to diffuse through the SEI layer (R_s), constant phase element (CPE-1), charge transfer resistance (R_{ct}), nonconstant phase element (CPE-2), and Warburg impedance (W). All the EIS spectra exhibited a semicircle in the high/medium frequency region, which is correlated to the resistance for lithium-ion diffusion through the SEI film (R_s) and the charge transfer resistance (R_{ct}). The –45° inclined line in the low frequency region is attributable to the Warburg impedance (W). As can be seen, the internal resistances for the samples are small, as reflected by the intercepts of the corresponding EIS spectra. The R_{ct} is a key indicator of the kinetics for all the samples. The charge-transfer resistances (R_{ct}) of the electrodes before cycling (Figure S11a, Supporting Information) and after rate capability measurements (Figure 5d; Figure S11b, Supporting Information), nearly corresponding to the diameter of the semicircle of EIS spectra, both decreased in the order of G, hG, N-G, and N-hG, further indicating the highest ionic conductivity for the N-hG. These results correlate well with their electrochemical performance.

In summary, we have developed a facile and scalable process for fabrication of N-hG with high electrochemical performance as an anode material in LIBs. The N-hG anode showed an initial discharge/charge capacity of 3056.1/989.5 mAh g^{-1} at 0.1 A g^{-1} in the voltage range of 0.02–2.5 V, with a maximum volumetric capacity of 384 mAh cm^{-3}. The N-hG electrode can be continuously deep cycled for 6000 cycles at 5 A g^{-1} in the voltage range of 0.02–2.5 V with a stable specific capacity of 553.5 mAh g^{-1}. Moreover, N-hG as an electrochemical capacitor delivered a higher maximum specific energy density of 445.9 Wh kg^{-1} and specific capacitance of 525 F g^{-1}, corresponding to a maximum volumetric energy density of 171.2 Wh L^{-1} and a volumetric capacitance of 201.6 F cm^{-3},

which are highly comparable to the best results previously reported on carbon-based electrode materials in capacitors with organic electrolytes. The excellent electrochemical performance of N-hG is attributable to its highly unstacked morphology with a large surface area of numerous N-doping-induced hole defects, which allow for an improved electrode/electrolyte wettability, ionic conductivity, and thermal stability. Thus, the simple method for preparing large quantities of N-hG provides a low cost carbon based electrode material with excellent electrochemical performance, making it attractive for the development of next-generation high-energy LIBs.

Supporting Information

Supporting Information is available from the Wiley Online Library or from the author.

Acknowledgements

The authors are grateful for financial support from AFOSR (FA9550-12-1-0037), NSF (CMMI-1400274, DMR-1106160). Y.L. and J.W.C. acknowledge the financial support from the Internal Research and Development (IRAD) program at NASA Langley Research Center. Y.L. is also grateful for the support from the Leading Edge Aeronautics Research for NASA (LEARN) program (Grant number NNX13AB88A).

[1] A. K. Geim, K. S. Novoselov, *Nat. Mater.* **2007**, *6*, 183.
[2] E. Yoo, J. Kim, E. Hosono, H.-S. Zhou, T. Kudo, I. Honma, *Nano Lett.* **2008**, *8*, 2277.
[3] a) D. Pan, S. Wang, B. Zhao, M. Wu, H. Zhang, Y. Wang, Z. Jiao, *Chem. Mater.* **2009**, *21*, 3136; b) A. L. M. Reddy, A. Srivastava, S. R. Gowda, H. Gullapalli, M. Dubey, P. M. Ajayan, *ACS Nano* **2010**, *4*, 6337.
[4] a) D. A. Brownson, D. K. Kampouris, C. E. Banks, *J. Power Sources* **2011**, *196*, 4873; b) Y. Gogotsi, P. Simon, *Science* **2011**, *334*, 917.
[5] X. Zhao, C. M. Hayner, M. C. Kung, H. H. Kung, *ACS Nano* **2011**, *5*, 8739.
[6] Z. Jiang, B. Pei, A. Manthiram, *J. Mater. Chem. A* **2013**, *1*, 7775.
[7] Z.-J. Jiang, Z. Jiang, *ACS Appl. Mater. Inter.* **2014**, *6*, 19082.
[8] X. Han, M. R. Funk, F. Shen, Y.-C. Chen, Y. Li, C. J. Campbell, J. Dai, X. Yang, J.-W. Kim, Y. Liao, J. W. Connell, V. Barone, Z. Chen, Y. Lin, L. Hu, *ACS Nano* **2014**, *8*, 8255.
[9] Z.-J. Jiang, Z. Jiang, W. Chen, *J. Power Sources* **2014**, *251*, 55.
[10] Y. Xu, Z. Lin, X. Zhong, X. Huang, N. O. Weiss, Y. Huang, X. Duan, *Nat. Commun.* **2014**, *5*, 4554.
[11] Y.-Y. Peng, Y.-M. Liu, J.-K. Chang, C.-H. Wu, M.-D. Ger, N.-W. Pu, C.-L. Chang, *Carbon* **2015**, *81*, 347.
[12] a) W. Yuan, Y. Zhou, Y. Li, C. Li, H. Peng, J. Zhang, Z. Liu, L. Dai, G. Shi, *Sci. Rep.* **2013**, *3*, 2248; b) A. Shen, Y. Zou, Q. Wang, R. A. Dryfe, X. Huang, S. Dou, L. Dai, S. Wang, *Angew. Chem. Int. Ed.* **2014**, *126*, 10980.
[13] Y. Lin, X. Han, C. J. Campbell, J.-W. Kim, B. Zhao, W. Luo, J. Dai, L. Hu, J. W. Connell, *Adv. Func. Mater.* **2015**, *25*, 2920.
[14] a) W. Chen, Y. Hu, J. Zhao, L. Zeng, X. Tao, *J. Mater. Chem. A* **2014**, *2*, 17415; b) Z. Xing, J. Tian, Q. Liu, A. M. Asiri, P. Jiang, X. Sun, *Nanoscale* **2014**, *6*, 11659; c) M. Patel, W. Feng, K. Savaram, M. R. Khoshi, R. Huang, J. Sun, E. Rabie, C. Flach, R. Mendelsohn, E. Garfunkel, H. He, *Small* **2015**, *11*, 3358.
[15] a) X. Li, H. Wang, J. T. Robinson, H. Sanchez, G. Diankov, H. Dai, *J. Am. Chem. Soc.* **2009**, *131*, 15939; b) L. Qu, Y. Liu, J.-B. Baek, L. Dai, *ACS Nano* **2010**, *4*, 1321; c) X. Wang, Q. Weng, X. Liu, X. Wang, D.-M. Tang, W. Tian, C. Zhang, W. Yi, D. Liu, Y. Bando, *Nano Lett.* **2014**, *14*, 1164; d) L. Zhan, S. Yang, Y. Wang, Y. Wang, L. Ling, X. Feng, *Adv. Mater. Interfaces* **2014**, *1*, 1300149; e) I. Y. Jeon, M. J. Ju, J. Xu, H. J. Choi, J. M. Seo, M. J. Kim, I. T. Choi, H. M. Kim, J. C. Kim, J. J. Lee, *Adv. Func. Mater.* **2015**, *25*, 1170; f) J. Xu, M. Wang, N. P. Wickramaratne, M. Jaroniec, S. Dou, L. Dai, *Adv. Mater.* **2015**, *27*, 2042; g) J. Hou, C. Cao, F. Idrees, X. Ma, *ACS Nano* **2015**, *9*, 2556.
[16] a) Z.-S. Wu, W. Ren, L. Xu, F. Li, H.-M. Cheng, *ACS Nano* **2011**, *5*, 5463; b) L. Qie, W.-M. Chen, Z.-H. Wang, Q.-G. Shao, X. Li, L.-X. Yuan, X.-L. Hu, W.-X. Zhang, Y.-H. Huang, *Adv. Mater.* **2012**, *24*, 2047; c) T. Hu, X. Sun, H. Sun, G. Xin, D. Shao, C. Liu, J. Lian, *Phys. Chem. Chem. Phys.* **2014**, *16*, 1060.
[17] a) T. Van Khai, H. G. Na, D. S. Kwak, Y. J. Kwon, H. Ham, K. B. Shim, H. W. Kim, *J. Mater. Chem.* **2012**, *22*, 17992; b) B. Kumar, M. Asadi, D. Pisasale, S. Sinha-Ray, B. A. Rosen, R. Haasch, J. Abiade, A. L. Yarin, A. Salehi-Khojin, *Nat. Commun.* **2013**, *4*, 2819.
[18] C. Villevieille, M. Ebner, J. L. Gómez-Cámer, F. Marone, P. Novák, V. Wood, *Adv. Mater.* **2015**, *27*, 1676.
[19] J. Xu, I. Y. Jeon, J. M. Seo, S. Dou, L. Dai, J. B. Baek, *Adv. Mater.* **2014**, *26*, 7317.
[20] a) A. Burke, *Electrochim. Acta* **2007**, *53*, 1083; b) M. D. Stoller, S. Park, Y. Zhu, J. An, R. S. Ruoff, *Nano Lett.* **2008**, *8*, 3498; c) C. Liu, Z. Yu, D. Neff, A. Zhamu, B. Z. Jang, *Nano Lett.* **2010**, *10*, 4863; d) Y. Zhu, S. Murali, M. D. Stoller, K. J. Ganesh, W. Cai, P. J. Ferreira, A. Pirkle, R. M. Wallace, K. A. Cychosz, M. Thommes, D. Su, E. A. Stach, R. S. Ruoff, *Science* **2011**, *332*, 1537; e) P. Simon, Y. Gogotsi, *Acc. Chem. Res.* **2013**, *46*, 1094; f) X. Yang, C. Cheng, Y. Wang, L. Qiu, D. Li, *Science* **2013**, *341*, 534; g) D. Yu, K. Goh, H. Wang, L. Wei, W. Jiang, Q. Zhang, L. Dai, Y. Chen, *Nat. Nano.* **2014**, *9*, 555.
[21] F. Zheng, Y. Yang, Q. Chen, *Nat. Commun*. **2014**, *5*, 5261.
[22] a) Z.-L. Wang, D. Xu, H.-G. Wang, Z. Wu, X.-B. Zhang, *ACS Nano* **2013**, *7*, 2422; b) R. Mukherjee, A. V. Thomas, D. Datta, E. Singh, J. Li, O. Eksik, V. B. Shenoy, N. Koratkar, *Nat. Commun.* **2014**, *5*, 3710.
[23] S. W. Lee, N. Yabuuchi, B. M. Gallant, S. Chen, B.-S. Kim, P. T. Hammond, Y. Shao-Horn, *Nat. Nano.* **2010**, *5*, 531.
[24] J. Xu, S.-L. Chou, Q.-f. Gu, H.-K. Liu, S.-X. Dou, *J. Power Sources* **2013**, *225*, 172.

Received: June 25, 2015
Revised: August 28, 2015
Published online: October 20, 2015

